

See discussions, stats, and author profiles for this publication at: <https://www.researchgate.net/publication/280256621>

Electrochemical performance of hematite nanoparticles derived from spherical maghemite and elongated goethite particles

ARTICLE *in* JOURNAL OF POWER SOURCES · FEBRUARY 2015

Impact Factor: 6.22 · DOI: 10.1016/j.jpowsour.2014.11.097

CITATIONS

6

READS

35

4 AUTHORS, INCLUDING:



Vanchiappan Aravindan

Nanyang Technological University

145 PUBLICATIONS 2,692 CITATIONS

SEE PROFILE



Electrochemical performance of hematite nanoparticles derived from spherical maghemite and elongated goethite particles



D. Maiti ^a, V. Aravindan ^b, S. Madhavi ^{b, c, **}, P. Sujatha Devi ^{a, *}

^a Nano-Structured Materials Division, CSIR-Central Glass and Ceramic Research Institute, Kolkata 700 032, India

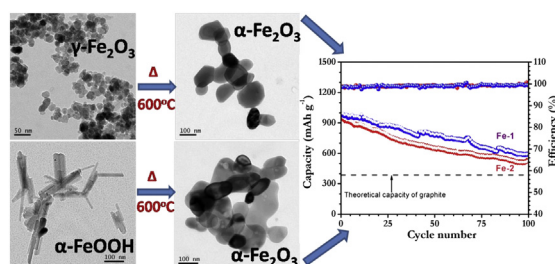
^b Energy Research Institute @ NTU (ERI@N), Nanyang Technological University, Singapore 63755, Singapore

^c School of Materials Science and Engineering, Nanyang Technological University, Singapore 639798, Singapore

HIGHLIGHTS

- α -Fe₂O₃ nanoparticles from maghemite nanoparticles and goethite rods.
- The α -Fe₂O₃ from maghemite exhibited a reversible capacity of ~1160 mAh g⁻¹.
- The α -Fe₂O₃ from goethite delivered a reversible capacity of ~1100 mAh g⁻¹.

GRAPHICAL ABSTRACT



ARTICLE INFO

Article history:

Received 12 August 2014

Received in revised form

20 October 2014

Accepted 21 November 2014

Available online 22 November 2014

Keywords:

Li-battery

Hematite

Reversible capacity

Nanoparticles

ABSTRACT

We report here an interesting observation on the electrochemical performance of hematite nanoparticles derived from cubic maghemite nanoparticles and hexagonal goethite rods prepared by a sonochemical process. We prepared hematite (α -Fe₂O₃) particles by annealing the as-prepared spherical cubic maghemite (γ -Fe₂O₃) nanoparticles and rod shaped hexagonal goethite (α -FeOOH) particles at 600 °C in air and investigated their performance as a Li-ion battery anode. Interestingly, annealing of spherical maghemite particles resulted in the formation of plate like interconnected hematite particles exhibiting unimodal pore distribution whereas rod shaped goethite has resulted in the formation of irregularly shaped porous hematite particles having a wide and multimodal pore distribution. The plate like α -Fe₂O₃ cells delivered a reversible capacity of ~1160 and the porous α -Fe₂O₃ nanoparticles exhibited a slightly lower capacity of ~1100 mAh g⁻¹. The test cells rendered a reversible capacity of ~926 and ~841 mAh g⁻¹ for nanoparticles derived from maghemite and goethite, respectively, after 40 galvanostatic cycles and a capacity of 611 and 522 mAh g⁻¹ at 0.1C rate after 100 cycles. In other words, the investigated α -Fe₂O₃ nanomaterials retained a reversible capacity of ~80 and 75%, respectively after 40 galvanostatic cycles. The basic difference in the electrochemical performance of the studied hematite particles have been attributed to the difference in the porosity of the samples. Moreover, the adopted synthesis technique is very simple and easily up scalable compared to most of the methods available in the literature for the synthesis of hematite nanoparticles.

© 2014 Elsevier B.V. All rights reserved.

* Corresponding author.

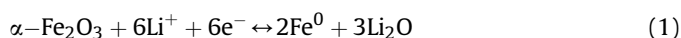
** Corresponding author. School of Materials Science and Engineering, Nanyang Technological University, Singapore 639798, Singapore; Energy Research Institute @ NTU (ERI@N), Nanyang Technological University, Singapore 63755, Singapore.

E-mail addresses: Madhavi@ntu.edu.sg (S. Madhavi), psujathadevi@cgcri.res.in, psujathadevi@gmail.com (P. Sujatha Devi).

1. Introduction

Hematite (α -Fe₂O₃) is an anti-ferromagnetic, n-type semi conducting material exhibiting unique properties such as non-toxicity,

low cost, high stability under ambient conditions and high resistance towards corrosion making it very attractive for lithium ion batteries (LIBs), gas sensors, catalysts, and adsorbents [1–6]. Owing to their novel properties leading to promising applications, interest in synthesizing hematite having different size and shape has been an area of current interest [7,8]. As an anode material in LIBs, α -Fe₂O₃ exhibits a high theoretical capacity of 1005 mAh g⁻¹. The performance of hematite in LIB's strongly depends on their structure, particle size, morphology and also to a larger extent on the porosity [9–14]. Nano-structured hematite has been demonstrated to have superior performance compared to bulk hematite exhibiting initial reversible capacities as high as 1303 mAh g⁻¹. This has been attributed to the effect of smaller particle size in decreasing the diffusion length of the Li-ions, apart from the pseudo-capacitance contribution from electrode/electrolyte interface [15]. It has also been found that porous electrode materials can facilitate the diffusion of Li-ions to active sites with less resistance and can also withstand the change of volume during the charge/discharge cycling [16–18]. Some recent investigations revealed the importance of shape of the hematite crystals in controlling the conversion reactions with Li-ions [19]. To achieve better performance with higher capacity and longer cycle life, different types of materials have been incorporated in hematite, to use them as alternative anodic materials for LIBs. For example, reduced graphene oxide (RGO)/ α -Fe₂O₃ composite used as anode in LIB exhibited higher discharge and charge capacities of 1693 and 1227 mAh g⁻¹, respectively [20,21]. Introduction of carbon coating or composite carbonaceous materials with hematite nanostructures also exhibited superior performance. The performance of LIB's is mainly governed by the reaction shown below [22,23].



In the initial stage, a small amount of Li could get inserted into the hexagonal hematite to form a hexagonal α -Li_xFe₂O₃. Further discharging reactions subsequently leads to the formation of metallic nanoparticles (Fe³⁺ to Fe²⁺ and Fe²⁺ to Fe⁰). Thus, the fine nanoclusters of Fe⁰ get dispersed in the amorphous Li₂O matrix. During charging Fe⁰ gets oxidized to Fe³⁺ resulting in the formation of γ -Fe₂O₃.

In the present work, we have compared the properties of hematite nanoparticles formed from two different host materials and their performance as anode material for LIB's. In our previous work, we had reported that drop-wise addition of hydrazine monohydrate (N₂H₄·H₂O) to an aqueous solution of 0.1 M ferric nitrate solution resulted in the formation of maghemite nanoparticles and simultaneous addition formed goethite nanorods [24]. In this work, we have prepared hematite (α -Fe₂O₃) particles exhibiting different properties by annealing the as-prepared spherical maghemite (γ -Fe₂O₃) nanoparticles and rod shaped goethite (α -FeOOH) particles at 600 °C in air. The electrochemical results indicated that the hexagonal plates derived from maghemite nanoparticles exhibit higher capacity and cycling stability than the hematite derived from goethite rods.

2. Experimental section

2.1. Synthesis of hematite nanoparticles

Ferric nitrate nonahydrate [Fe(NO₃)₃·9H₂O] GR, ethanol GR were purchased from Merck, Germany and hydrazine monohydrate (N₂H₄·H₂O) was purchased from Merck, India. The detailed synthesis of maghemite and goethite has been discussed in our previous work. [24] In brief, drop-wise addition of hydrazine monohydrate to an aqueous solution of 0.1 M ferric nitrate resulted

in the formation of maghemite whereas on simultaneous addition of hydrazine monohydrate, goethite was formed. The as prepared powders were calcined at 600 °C in a muffle furnace for 4 h at a heating rate of 60 °C/hour in air. After the heat treatment, the brownish black maghemite and the light yellow goethite were transformed into red hematite nanoparticles. The hematite nanoparticles prepared from maghemite and goethite will be designated as Fe-M and Fe-G, respectively, in the rest of the manuscript.

2.2. Structural characterization

The X-ray diffraction patterns were collected between 5° and 80° (2 θ) in a Philips X-ray diffractometer equipped with CuK α radiation (λ = 1.5406 Å) at a 2 θ scan rate of 2° min⁻¹. The particle size and shape were determined on a Tecnai G2 Transmission Electron Microscope (TEM) operating at 300 kV. The local crystallographic structure was studied by high resolution transmission electron microscopic (HR-TEM) studies. The dispersion for TEM analysis was prepared by sonicating a small amount of the powder in ethanol for 20 min. UV-visible analysis was carried out on a Shimadzu UV-Vis-NIR spectrometer UV-3600. Raman spectra were acquired on a Renishaw InVia Reflex micro Raman spectrometer with excitation of argon ion (514 nm) lasers and the spectra were collected with a resolution of 1 cm⁻¹. Nitrogen adsorption-desorption measurements were carried out at 77 K with a Quantachrome (ASIQ MP, Quantachrome, Boynton Beach, FL) instrument. The powders were degassed under vacuum at 250 °C for 4 h for the measurement. The surface area was obtained using Brunauer-Emmet-Teller (BET) method within the relative pressure (P/Po) range 0.05–0.20, and the pore size distribution (PSD) was calculated by Barret-Joyner-Halenda (BJH) method. The nitrogen adsorption volume at the relative pressure (P/Po) of 0.99 was used to determine the pore volume.

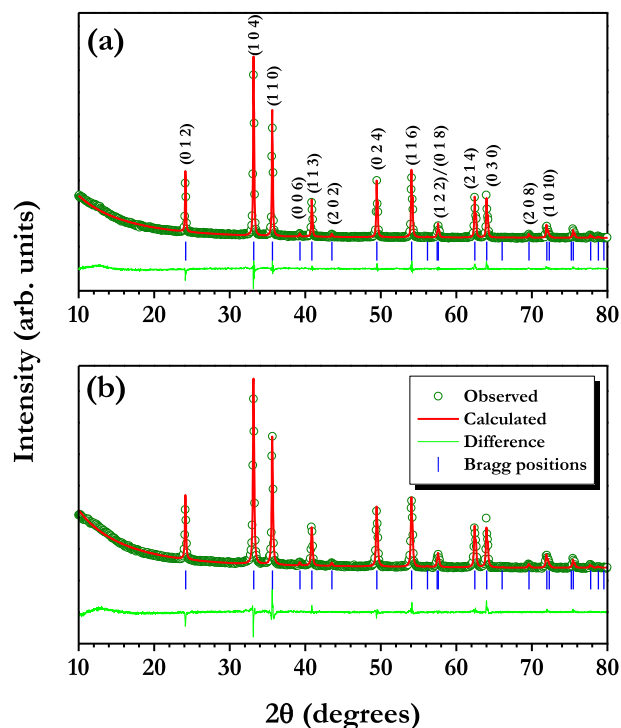


Fig. 1. Rietveld refined powder X-ray diffraction pattern of Fe₂O₃ hematite nanoparticles obtained from (a) maghemite- γ -Fe₂O₃ and (b) goethite- α -FeOOH.

2.3. Electrochemical characterization

All the electrochemical studies were performed in standard two electrode coin-cell (CR 2016) configuration. The composite electrode was formulated with accurately weighed active material (10 mg, α -Fe₂O₃), conductive additive (Super P, 2 mg) and binder (Teflonized acetylene black, TAB-2, 2 mg) using ethanol. Then, the mixture was pressed over 200 mm² stainless steel mesh which acts as current collector, and subsequently dried at 60 °C for overnight under vacuum conditions before conducting coin-cell assembly under Ar filled glove box. The test cells were composed of composite α -Fe₂O₃ electrode as an anode and metallic lithium as counter/reference electrode, which were separated by microporous glass fiber separator (Whatman, Cat. No. 1825 047, UK). The 1 M LiPF₆ in ethylene carbonate (EC):di-methyl carbonate (DMC) (Selectipur LP 30, Merck KGaA, Germany) mixture was used as the electrolyte solution. Cyclic voltammetry (CV) studies were carried out on a Solartron 1470E and SI 1255B Impedance/gain-phase analyzer coupled with a potentiostat at slow scan rate of 0.1 mV s⁻¹. Galvanostatic charge–discharge studies were conducted using Arbin battery tester (BT 2000) at ambient temperature conditions between 0.005 and 3 V vs. Li at different current densities.

3. Results and discussion

3.1. X-ray diffraction analysis

In Fig. 1, the Rietveld refined Powder X-ray diffraction (XRD) patterns of the red powders obtained on annealing maghemite and goethite nanoparticles are presented. The XRD patterns compared well with the hexagonal structure of hematite (α -Fe₂O₃) reported in JCPDS file No. 33-0664 corresponding to bulk α -Fe₂O₃ phase. From the Rietveld refinement, it could be confirmed that the red powders formed in both cases were α -Fe₂O₃. No undecomposed phase such as γ -Fe₂O₃ or α -FeOOH was observed in the XRD pattern as evident from Fig. 1. The calculated lattice parameters are presented in Table 1. The hematite formed from goethite (Fe–G) exhibited a slightly higher lattice volume compared to the one formed from maghemite (Fe–M). On heating goethite at 600 °C, the hematite phase was formed due to the removal of water as shown in Equation (2).



On the other hand, the formation of hematite from maghemite was due to the normal crystallographic phase transformation [25]. The mean crystallite sizes of the hematite powders calculated from the XRD Scherer formula, applied to (104) reflection of hematite were 105.9 nm and 70.9 nm, respectively, for Fe–M and Fe–G, respectively.

3.2. Morphological characterization

In Figs. 2 and 3, the TEM images of hematite nanoparticles obtained from maghemite (Fe–M) and goethite (Fe–G) are presented

along with the TEM of the starting materials. The starting material maghemite consists of spherical particles with a mean size of ~21.19 nm. On heating, the spherical maghemite particles (Fig. 2a) changed their geometry and size as evident from Fig. 2b,c. The converted hematite nanograins exhibited a thin hexagonal plate like morphology compared to the starting spherical maghemite nanoparticles. It is interesting to observe the many fold increase in size from 21.19 nm for the maghemite to around 106 nm for the resulting hematite. On the other hand, the rod shaped α -FeOOH with an aspect ratio of around 14, changed the initial shape during phase transformation resulting in slightly elongated irregularly shaped porous particles.

It is interesting to note the formation of well defined disordered smaller and larger pores in various diameters in Fe–G, during the decomposition and subsequent formation of goethite (Fig. 3b–d and Supporting Information, Fig. S1a). The generation of pores could be due to the removal of water from α -FeOOH as shown in Equation (2). The pores are also present in the Fe–M samples, but in very low volumes (shown by red circles (in web version) in Fig. 2c) formed by the decomposition of small amount of goethite present in the as-prepared maghemite as revealed by the synchrotron X-ray studies [24]. The distribution of the particles of Fe–M is shown in Fig. 2e. The average size of Fe–M nanoparticles was 106 nm. As mentioned previously, the calculated crystallite sizes (from XRD) were 105.9 and 70.9 nm, respectively, for Fe–M and Fe–G. Thus, the crystallite size calculated from the XRD line broadening is almost identical to the particle size obtained from the TEM data in the case of Fe–M sample, indicating that each particle is a single crystal of α -Fe₂O₃. In the case of Fe–G, the crystallite size calculated from the XRD line broadening could not be compared with the TEM particle size due to their elongated shape and irregular size. In Figs. 2d and 3e, the selected area diffraction patterns obtained from Fe–M and Fe–G particles, respectively, are presented indicating the high crystalline nature of the derived particles. The high resolution (HR) TEM images of the Fe–M and Fe–G are presented in Figs. 2f and 3f respectively. The HRTEM confirms the formation of well developed lattice fringes ensuring the monocrystalline nature of the individual particles. The distance between adjacent lattice fringes measured as 2.72 Å (Fig. 2f) corresponds to the 104 reflection of α -Fe₂O₃. The elongated particles of Fe–G may be having more than one crystallite as revealed from the HRTEM picture shown in Fig. 3f where both 104 and 012 reflections are evident. In addition, the presence of Moiré pattern indicating overlapping planes and the presence of large pores are also evident in the HRTEM shown in the supporting information (Supporting Information, Fig. S1b).

3.3. Raman and UV–Vis spectroscopic studies

We have also carried out Raman spectroscopic studies to further identify the crystal phase and nature of Fe₂O₃. In Fig. 4a, the Raman spectra of the hematite nanoparticles, Fe–M and Fe–G are presented. The spectra contain six Raman bands 224, 244, 292, 408, 493 and 608 cm⁻¹ which are due to transversal optical (TO) mode of hematite [26]. The peaks at 245 and 493 cm⁻¹ are attributed to the A_{1g} modes. The other four peaks at 244, 292, 408 and 608 cm⁻¹ are assigned to the E_g mode. In the Raman spectra, the peaks of

Table 1
Characteristics of the studied hematite Nanoparticles.

Sample id	Host matrix/shape	Lattice parameters a (Å), c (Å)	Unit cell volume (Å) ³	Crystallite size (nm)	Particle size (nm)	Surface area (m ² /gm)	Pore volume (cc/g)
Fe-M	γ -Fe ₂ O ₃	5.0336(2)	301.64(4)	105.9	106	8.40	0.2044
	Spherical	13.7468(4)					
Fe-G	α -FeOOH	5.0336(7)	301.67(7)	70.9	121	9.57	0.2651
	Rod	13.7480(8)					

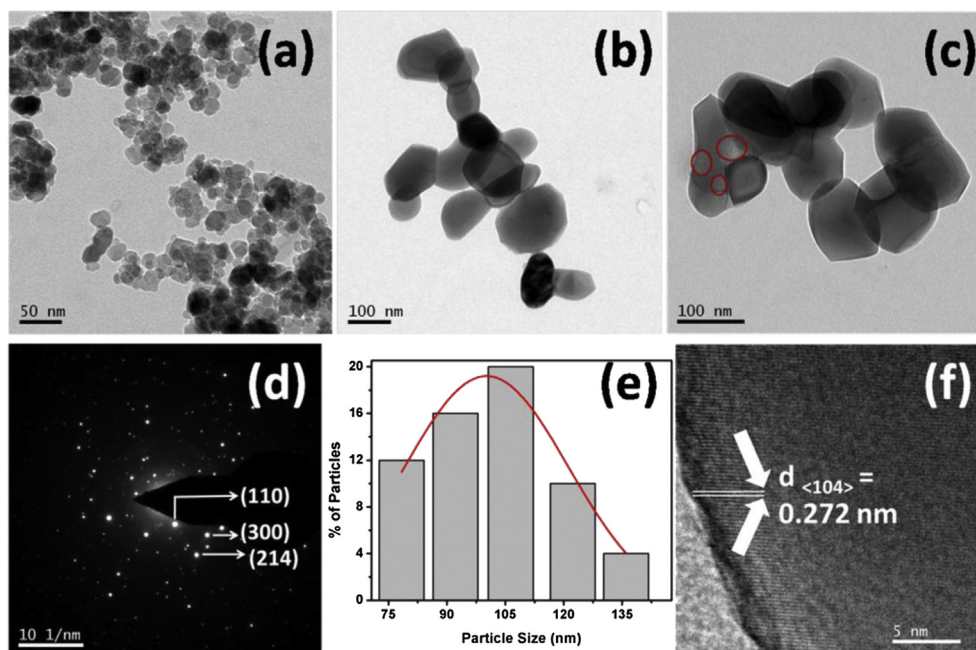


Fig. 2. TEM bright field images of (a) maghemite (b, c) hematite derived from maghemite, Fe–M (d) SAED pattern (e) histogram of (b) and (f) HRTEM image from a single particle.

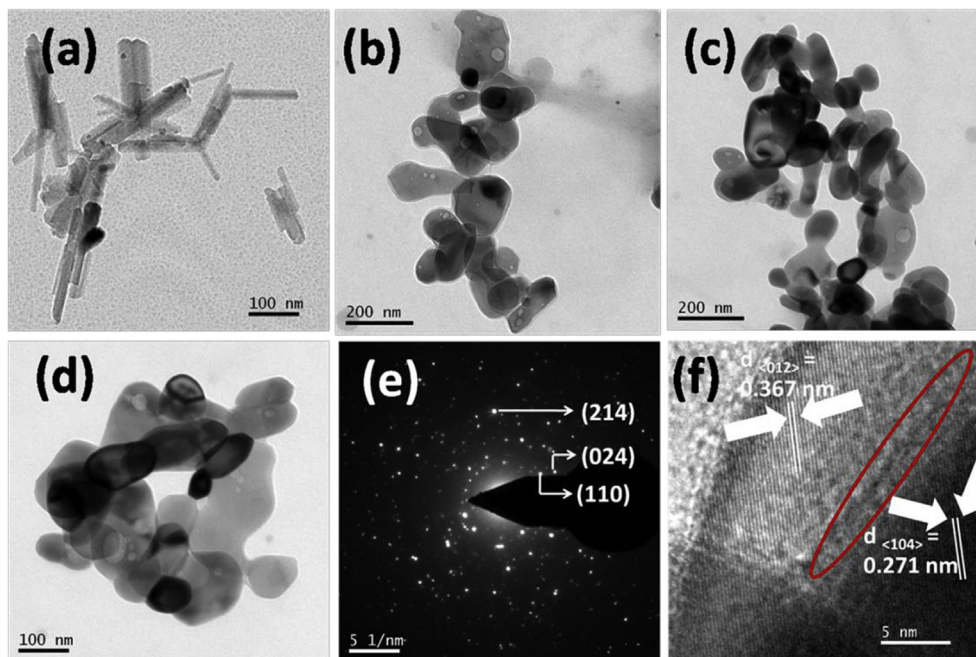


Fig. 3. TEM bright field images of (a) goethite rods- α -FeOOH (b–d) hematite particles derived from goethite with clear indication of pores (e) SAED pattern from (d) and (f) HRTEM image indicating two different overlapping crystal planes.

Fe–M, looks broader and shifted towards higher wave numbers as shown in the Supporting Information, Fig. S2, due to its smaller particle size. The four Raman peaks at 224, 244, 408 and 608 cm^{-1} shifted towards higher wavenumbers for Fe–M compare to Fe–G as shown in Fig. S2. The peak broadening and shifting of Raman bands towards higher wavenumbers due to smaller particles has been reported by others [27,28]. We also observed higher FWHM for smaller particles Fe–M particles compared to Fe–G particles. Further, the appearance of a new peak at 668 cm^{-1} in the spectra of Fe–M indicates the presence of lattice defects and disorder. The

optical properties of the synthesized hematite nanoparticles were also carried out at room temperature by UV-visible spectroscopy (Fig. 4b). The band gap of the samples was calculated from the absorption data shown in Fig. 4b. The graph shown in Fig. 4b shows an intense band around 240 nm and a broad band in the 350–600 nm range. The absorption bands in the ultraviolet region from 200 to 400 nm are assigned to the ligand to metal charge transfer transition [29]. The calculated band gaps of Fe–M and Fe–G were 2.21 and 2.23 eV, respectively, which are in good agreement with the bulk band gap value, 2.2 eV for n-type α -Fe₂O₃.

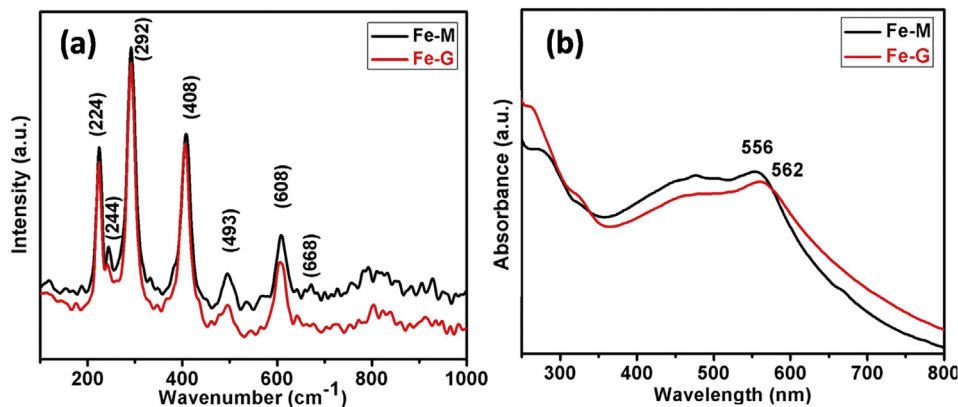


Fig. 4. (a) Raman spectra and (b) UV-Visible spectra of hematite nanoparticles obtained from maghemite (Fe–M) and goethite (Fe–G), respectively.

[30,31]. The visible absorption maxima were observed at 556 and 562 nm, respectively, for Fe–M and Fe–G particles [32]. A slight shift in the absorption band maxima of the two hematite nanoparticles is assigned to the difference in size of the two samples.

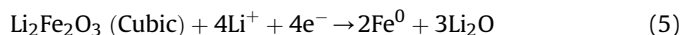
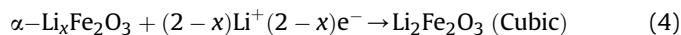
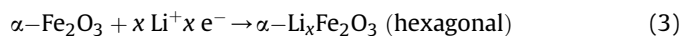
3.4. Magnetic measurements

In order to further characterize the prepared hematite particles, we have carried out the magnetic measurements at room temperature. The Fe–M and Fe–G samples exhibited saturation magnetization moments of 0.4 and 0.23 emu/g, respectively. Both the samples exhibited a weak hysteresis loop with coercivities of 91 and 27 Oe, respectively at RT indicating the existence of weak ferromagnetism in α -Fe₂O₃ (Supporting Information Fig. S3). The high coercivity value of Fe–M could be due to the high magneto-crystalline anisotropy exhibited by hexagonal microstructures [33].

3.5. Cyclic voltammetry (CV) studies

Fig. 5 represents the CV traces of α -Fe₂O₃ nanostructures in half-cell configuration (Li/ α -Fe₂O₃) between 0.005 and 3 V vs. Li at a scan rate of 0.1 mV s⁻¹. Both Fe–M and Fe–G exhibited a strong and

prominent peak at ~0.65 V vs. Li and broad peak at ~1.67 V vs. Li during first cathodic and anodic sweeps, respectively. As clear from Fig. 5, during the cathodic polarization in the first cycle, a prominent peak was observed at 0.65 V (step 3) with two small peaks appears at 0.81 V (step 2) and 1.62 V (step 1) indicating the following lithiation steps.



As clear from the small peak around 1.62 V, a small amount of lithium can be inserted into the crystal structure of the as-prepared hematite without any change in structure resulting in the irreversible Li-insertion in to the hematite phase and formation of Li_xFe₂O₃ phase (Equation (3)) [34]. In the next step the hexagonal α -Li_xFe₂O₃ is transformed to cubic Li₂Fe₂O₃ as evident from the weak peak at 0.81 V (Equation (4)) [35–38]. It is interesting to note that step 2 corresponding to the hexagonal α -Li_xFe₂O₃ to cubic Li₂Fe₂O₃ is not very prominent in Fe–G sample. The strong peak at 0.65 V corresponds to the complete reduction of iron from Fe²⁺ to Fe⁰ and the decomposition of the electrolyte (Step 3, Equation (5)). The amount of Li-insertion was found to be ~1.57 and ~1.87 mol for Fe–M and Fe–G, respectively. The oxidation of metallic nanoparticles takes place at ~1.67 V vs. Li during subsequent anodic scan. Strictly speaking, two oxidation peaks were observed at ~1.67 and ~1.94 V vs. Li, which is due to the oxidation of Fe⁰ into Fe²⁺ and subsequent oxidation of Fe²⁺ into Fe³⁺, respectively. In the successive cycles, redox reactions occurred in reversible manner at ~0.83 and ~1.69 V vs. Li during cathodic and anodic scans, respectively. Overlapping of CV traces during cycling suggests the excellent reversibility of hematite nanostructures in half-cell assembly. The overall electrochemical reaction is similar to that is shown in Equation (6). The marginal increase in the area underneath the curve for nanoplates Fe–M corresponds to the higher specific capacity of the former compared to the more porous elongated particles.

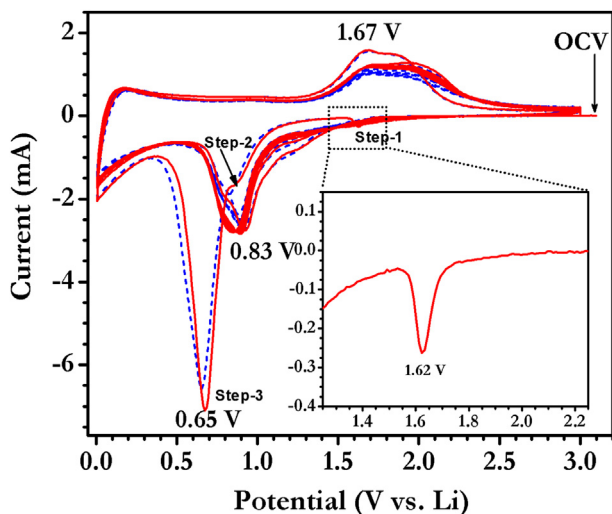


Fig. 5. Cyclic voltammetry traces of Fe₂O₃ nanostructures in half-cell configuration (Li/Fe₂O₃) between 0.005 and 3 V vs. Li at slow scan rate of 0.1 mV s⁻¹, in which metallic Li acts as both counter and reference electrode. Solid and dotted line corresponds to Fe–M and Fe–G, respectively.

3.6. Potential vs. capacity measurement

Galvanostatic charge–discharge profiles are conducted for hematite nanoparticles between 0.005 and 3 V vs. Li at current density

of 100 mA g^{-1} as illustrated in Fig. 6. The test cells delivered a reversible capacity of ~ 1160 and $\sim 1100 \text{ mAh g}^{-1}$, respectively, for the Fe–M and Fe–G. The observed capacities are highly reproducible with deviation of $\pm 15 \text{ mAh g}^{-1}$ irrespective of the nanostructures. As expected, irreversible capacity is a big issue for the conversion type anodes [1]. Irreversible capacity of ~ 616 and $\sim 542 \text{ mAh g}^{-1}$ was noted for the above two samples. During lithiation (discharge) process, Li-insertion in to hematite phase has been clearly evidenced from ~ 1.7 to $\sim 1.2 \text{ V}$ vs. Li ($\text{Li}_{0.25}\text{Fe}_2\text{O}_3$) and further Li-insertion was also noted between ~ 1.2 and $\sim 0.8 \text{ V}$ vs. Li range (shown by circle in Fig. 6a). There is not much variation in the Li-insertion in the former range, but the insertion of ~ 1.62 and $\sim 1.32 \text{ mol}$ of Li was noted for Fe–M and Fe–G, respectively. As a result, increase in Li-cyclability is noted for the less porous hematite derived from maghemite nanoparticles compared with more porous hematite derived from one dimensional goethite nanorods. A long distinct plateau $\sim 0.8 \text{ V}$ vs. Li is associated with the structural destruction along with electrolyte decomposition. The observed capacity is slightly higher than the theoretical capacity of $\sim 1007 \text{ mAh g}^{-1}$ for cycleable 6 mol of Li. The higher specific capacity is mainly due to the non-faradaic mechanism called pseudo-capacitance which is an interfacial reaction because of the charge separation across the metal/ Li_2O phase boundary. Similar kind of higher specific capacity is noted by other researchers as well, for example Cherian et al. [11], reported the reversible capacity of $\sim 1095 \text{ mAh g}^{-1}$ for one dimensional nanorods prepared by electrospinning technique. Chou et al. [23] also reported a higher reversible capacity of $\sim 1210 \text{ mAh g}^{-1}$ for hollow structured Fe_2O_3 . Reversible capacity of $\sim 1227 \text{ mAh g}^{-1}$ was reported by Zhu et al. [20] for reduced graphene oxide/ Fe_2O_3 hybrid system. Spherical shaped Fe_2O_3 /graphene composite delivered the charge capacity of 1210 mAh g^{-1} . A plot of capacity vs. cycle number for the two

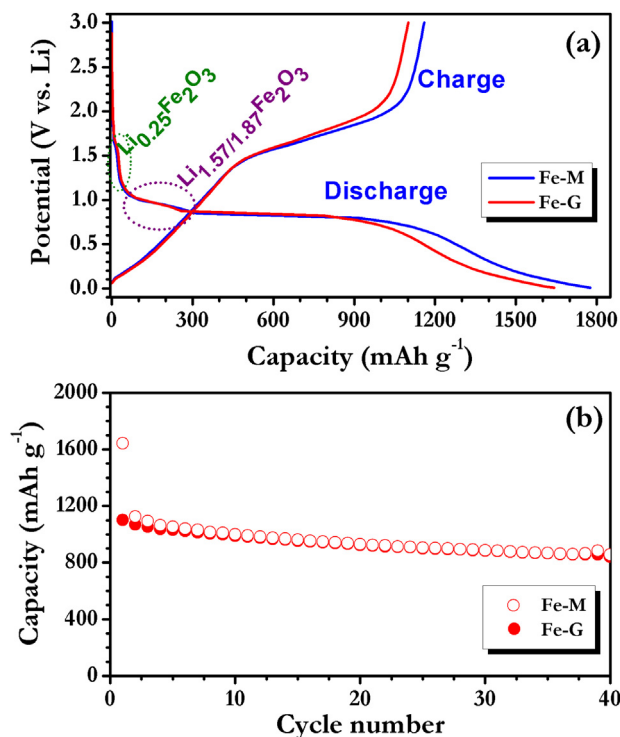


Fig. 6. (a) Initial galvanostatic charge–discharge curves of Fe_2O_3 nanostructures in half-cell configuration ($\text{Li}/\text{Fe}_2\text{O}_3$) between 0.005 and 3 V vs. Li at constant current density of 100 mA g^{-1} , and (b) Plot of capacity vs. cycle number, in which open and solid symbols corresponds to discharge and charge capacity, respectively.

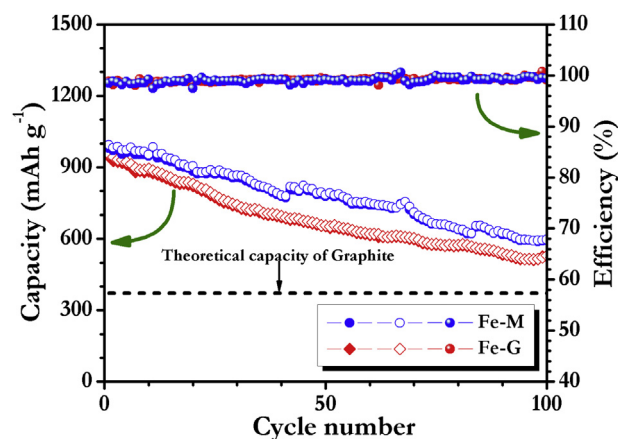


Fig. 7. Cycling profiles of the Fe_2O_3 nanostructures at current density of 500 mA g^{-1} between 0.005 and 3 V vs. Li at ambient temperature. Open, half-filled and spheres correspond to the charge capacity, discharge capacity and efficiency, respectively.

hematite phase materials with different morphologies are shown in Fig. 6b. Both, materials displayed a very stable cycling behavior for the tested 40 cycles. The test cell renders a reversible capacity of ~ 926 and $\sim 841 \text{ mAh g}^{-1}$, respectively, for Fe–M and Fe–G after 40 galvanostatic cycles. In other words, the investigated nanomaterials retained the reversible capacity of ~ 80 and 75% , respectively, after 40 cycles. The observed cyclability is one of the best values reported on hematite phase materials compared to that has been reported by many investigators, Cherian et al. [11], Wang et al. [39], Chou et al. [23], Zhu et al. [20] and Reddy et al. [1]. In order to further evaluate the long term cyclability of the materials under study, we have also carried out long-term cyclability for 100 cycles at a current density of 500 mA g^{-1} and is given in Fig. 7 along with the coulombic efficiency. The coulombic efficiencies remained $>98\%$ between 1 and 100 cycles irrespective of the precursors. As expected, a slightly higher decrease in capacity trends are noted for both kinds of hematite nanostructures compared to low current rates (100 mA g^{-1}) which is mainly attributed to the inferior electronic conductivity of the native phase materials. After 100 cycles, the discharge capacity of Fe–M was $\sim 611 \text{ mAh g}^{-1}$ and that of Fe–G was $\sim 522 \text{ mAh g}^{-1}$ which are still higher than the theoretical capacity of currently used graphite ($\sim 372 \text{ mAh g}^{-1}$). Most of the reports on the charge–discharge performance of $\alpha\text{-Fe}_2\text{O}_3$ are restricted to 50 to 60 cycles [40–42]. Our samples exhibited a higher cycling capacity compared to many of the reported data shown in Table 2. We have tested our samples down to 250 cycles where the fading was more evident for Fe–G than Fe–M samples (Supporting Information Fig. S4).

3.7. Rate performance study

Rate performance is another important criterion to employ them as prospective anode material for high performance applications like electric/hybrid electric vehicles. Rate capability studies were performed for both hematite nanostructures in ambient conditions and illustrated in Fig. 8. Apparent to note that, decrease in capacity trends are noted when increasing the current density irrespective of the sample nature. Obvious difference between the electrochemical profiles is noted for the samples between the current density of $0.25\text{--}1 \text{ A g}^{-1}$ ($0.25\text{--}1\text{C}$) when both nanostructures exceed beyond 1 A g^{-1} delivered almost same capacity profile. The decrease in capacity during increase in current rate is due to the lower participation of the electro-active material/or surface of the active material only involved in the electrochemical

Table 2
Electrochemical performance comparison of different α -Fe₂O₃ nanoparticles.

Morphological Character	Size	Pore Size (nm)	Long-term cycling (mAh g ⁻¹)	Experimental conditions nth cycle/rate, C	Ref
Cube	Hollow	1.5 μ m	—	457	[38]
	Solid	—	177	100/0.1	
Sphere	Hollow	~1 μ m	2–15	710	[39]
	Solid	—	340	30/0.1	
Spindle Bulk	—	~1.3 μ m	<10	911	[19]
	—	—	630	50/0.2	
Nanoflake	—	—	680	50/0.1	[13]
Nanotube	—	200 nm	510	50/0.1	[10]
Sphere	Hollow	~500 nm	863	50/0.1	[12]
	Solid	—	578	—	
Melon like	—	~150 nm	15.02	662	[40]
Nanospindle	Hollow	500 nm	—	456	[41]
	—	120 nm (along major axis)	—	—	
	—	120 nm (along minor axis)	—	—	—
Microsphere	—	1 μ m	396	—	This work
Plates	—	106 nm	59	926	
	—	—	—100	—	—
Elongated	—	30	841	40/0.1	This work
	—	—100	—	—	
	—	—	601	100/0.5	—
	—	—	481	—	—

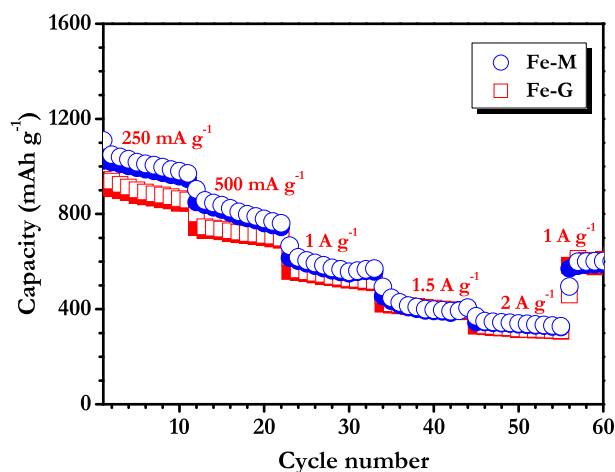


Fig. 8. Rate performance studies of hematite nanostructures in half-cell assembly between 0.005 and 3 V vs. Li at various current densities.

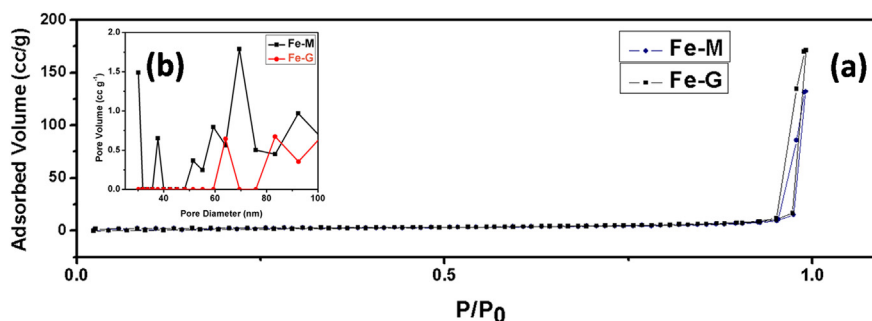


Fig. 9. Nitrogen adsorption–desorption isotherms (a) and (b) Barrett–Joyner–Halenda pore size distribution plot of Fe–M and Fe–G samples.

reaction. However, meager capacity fade is encountered during such high current operations in both cases. The observed capacity values are comparable to the previous report on the electrochemical performance of Fe₂O₃ anodes described in the extensive review by Reddy et al. [1]. Further studies are in progress to suppress the irreversible capacity loss and to mitigate the capacity fade.

3.8. Electrochemical impedance studies

Nyquist plots of the ac impedance collected in the open circuit voltage stage for Fe–M and Fe–G samples are shown in the Supporting Information Fig. S5. Both samples exhibited a semicircle composed of three main regions likely high frequency region which is associated with solution resistance. The medium frequency region is corresponds to the charge-transfer (CT) resistance and vertical tail inclined at 45° is ascribed to the Li-diffusion in to the active material. As expected, the diameter of the semicircle *i.e.* CT resistance for Fe–M is smaller than that of Fe–G (Fe–M exhibited a charge transfer resistance of 24.18 Ω and Fe–G exhibited a resistance of 29.47 Ω). The lower CT resistance certainly provides the improved electrochemical activity of the hematite phase obtained from spherical maghemite particles.

It is noteworthy to observe the enhanced capacity and cycling performance of hematite derived from spherical maghemite electrode (Fe–M) compared to the elongated particles (Fe–G) formed from rod shaped goethite particles. The XRD, Raman and optical characterization of both Fe–M and Fe–G confirmed the structural and chemical identity of both the samples as α -Fe₂O₃. On the other hand, microscopic investigations showed difference in the morphology and texture of the investigated samples. Now, having demonstrated a difference in the electrochemical performance in spite of having structural and chemical uniformity, we have carried out surface area and porosity measurements on Fe–M and Fe–G samples in order to ascertain the above mentioned difference in the electrochemical performance of hematite nanoparticles. We have carried out the porosity measurements by the Nitrogen adsorption–desorption of Fe–M and Fe–G samples. The N₂ isotherms of the Fe–M and Fe–G samples are presented in Fig. 9a and the respective pore-size distribution (PSD) plots calculated from the desorption branches of the nitrogen sorption isotherms are shown in Fig. 9b as an inset. The N₂ adsorption–desorption isotherms are of typical type IV isotherm with a distinct hysteresis loop as evident in Fig. 9a, indicating their mesoporous nature. This type of isotherms usually occurs on porous adsorbents with pores in the range of 1.5–100 nm. At higher pressures the slope shows increased up-take of adsorbate as pores become filled and inflection point typically occurs near completion of the first monolayer. In our samples,

the hysteresis loop (inflection point) of Fe–M begins at (P/P_0) around 0.953 while that of Fe–G starts at a slightly lower relative pressure of 0.951. It is interesting to note that the pore size distribution is centered at a single peak at 64 nm for Fe–M with the pore size ranging from 59 to 100 nm. The PSD of Fe–G sample, on the other hand, exhibited a multi modal wide distribution of pores ranging from 30 nm to as high as 100 nm with peak maxima at 30, 37, 52, 59 and 70 nm, respectively. Thus, the pore size distribution of the two samples exhibited a distinct difference from single modal uniform distribution for Fe–M to multimodal wider distribution for Fe–G hematite samples. The presence of mesopores and macro pores in Fe–G (Supporting Information Fig. S1a) and only macropores in Fe–M are in good agreement with the TEM data shown in Figs. 3 and 2, respectively. The pore volume also increased from 0.2044 cc g⁻¹ to 0.2659 cc g⁻¹ for the Fe–M and Fe–G samples, respectively. The Brunauer–Emmett–Teller (BET) surface areas of the nanostructured hematite derived from Fe–M and Fe–G were 8.4 m² g⁻¹ and 9.567 m² g⁻¹, respectively. In spite of having different morphology and particle size, both the samples exhibited almost similar surface area. However, the wider distribution of pores and an uneven shape may cause heterogeneous reactive sites for redox reactions in and out of the particles resulting in lower capacity of Fe–G compared to Fe–M sample. The small sized interconnected plate like grains and uniform size and pore distribution of Fe–M nano particles on the other hand could benefit an enhanced performance. In addition, the lower charge transfer resistance exhibited by Fe–M also helps in the improved electrochemical activity of the hematite phase obtained from spherical maghemite particles.

4. Conclusion

Maghemite (γ -Fe₂O₃) nanoparticles and goethite (α -FeOOH) nanorods, formed during the sonication of ferric nitrate solution, on annealing at 600 °C has resulted in the formation of α -Fe₂O₃ exhibiting diverse shapes and porosity. Interestingly, the annealing of spherical maghemite resulted in the formation of plate like interconnected hematite particles where as rod shaped goethite has resulted in the formation of irregularly shaped highly porous hematite particles. On testing as anode materials for Li-battery, the plate like α -Fe₂O₃ test cells delivered a reversible capacity of ~1160 and the porous α -Fe₂O₃ nanoparticles delivered a capacity of ~1100 mAh g⁻¹. The test cell renders a reversible capacity of ~926 and ~841 mAh g⁻¹ for nanoparticles derived from γ -Fe₂O₃ and α -FeOOH, respectively, after 40 galvanostatic cycles. The wider distribution of pores and an uneven shape of goethite derived hematite particles may cause heterogeneous reactive sites for redox reactions in and out of the particles resulting in lower capacity. On the other hand, the small and uniform sized interconnected dense plate like grains with uniform pore distribution of maghemite derived hematite particles has helped in enhanced performance and high capacity.

Acknowledgment

PSD thanks CSIR Chemical Science Cluster Program on MULTI-FUN, CSC 0101 for financial support. VA and SM thank the National Research Foundation (NRF, Singapore) for financial support through the Competitive Research Programme (CRP, Grant no. NRF-CRP4-2008-03). DM is indebted to the Council of Scientific and Industrial Research (CSIR), Govt. of India for the award of Senior Research

Fellowship through the National Eligibility Test. PSD also acknowledges the Electron Microscopy Section of CSIR-CGCRI for assistance in recording the TEM pictures.

Appendix A. Supplementary data

Supplementary data related to this article can be found at <http://dx.doi.org/10.1016/j.jpowsour.2014.11.097>.

References

- [1] M.V. Reddy, G.V. Subba Rao, B.V.R. Chowdari, Chem. Rev. 113 (2013) 5364.
- [2] H.G. Cha, S.J. Kim, K.J. Lee, M.H. Jung, Y.S. Kang, J. Phys. Chem. C 115 (2011) 19129.
- [3] S. Zeng, K. Tang, T. Li, Z. Liang, D. Wang, Y. Wang, Y. Qi, W. Zhou, J. Phys. Chem. C 112 (2008) 4836.
- [4] Y. Yang, H. Ma, J. Zhuang, X. Wang, Inorg. Chem. 50 (2011) 10143.
- [5] Y. Zheng, Y. Cheng, Y. Wang, F. Bao, L. Zhou, X. Wei, Y. Zhang, Q. Zheng, J. Phys. Chem. B 110 (2006) 3093.
- [6] Y. Cheng, B. Zou, C. Wang, Y. Liu, X. Fan, L. Zhu, Y. Wang, H. Ma, X. Cao, Cryst. Eng. Comm. 13 (2011) 2863.
- [7] W. Dong, C. Zhu, J. Mater. Chem. 12 (2002) 1676.
- [8] L. Li, Y. Yu, F. Meng, Y. Tan, R.J. Hamers, S. Jin, Nano Lett. 12 (2012) 724.
- [9] Y.Y. Fu, R.M. Wang, J. Xu, J. Chen, Y. Yan, A.V. Narlikar, H. Zhang, Chem. Phys. Lett. 379 (2003) 373.
- [10] J. Chen, L. Xu, W. Li, X. Gou, Adv. Funct. Mater. 17 (2005) 582.
- [11] C.T. Cheriai, J. Sundaramurthy, M. Kalavani, P. Ragupathy, P. Suresh Kumar, V. Thavasi, M.V. Reddy, Chong Haur Sow, S.G. Mhaisalkar, S. Ramakrishna, B.V.R. Chowdari, J. Mater. Chem. 22 (2012) 12198.
- [12] B. Wang, J.S. Chen, X.W. Lou, J. Mater. Chem. 22 (2012) 9466.
- [13] Y. Song, S. Qin, Y. Zhang, W. Gao, J. Liu, J. Phys. Chem. C 114 (2010) 21158.
- [14] M.V. Reddy, T. Yu, C.H. Sow, Z.X. Shen, C.T. Lim, G.V.S. Rao, B.V.R. Chowdari, Adv. Funct. Mater. 17 (2007) 2792.
- [15] S. Chaudhari, M. Srinivasan, J. Mater. Chem. 22 (2012) 23049.
- [16] D. Larcher, C. Masquelier, D. Bonnin, Y. Chabre, V. Masson, J.B. Leriche, J.M. Tarascon, J. Electrochem. Soc. 150 (2003) A133.
- [17] B. Sun, J. Horvat, H.S. Kim, W.S. Kim, J. Ahn, G. Wang, J. Phys. Chem. C 114 (2010) 18753.
- [18] B. Koo, H. Xiong, M.D. Slater, V.B. Prakapenka, M. Balasubramanian, P. Podsiadlo, C.S. Johnson, T. Rajh, E.V. Shevchenko, Nano Lett. 12 (2012) 2429.
- [19] X. Xu, R. Cao, S. Jeong, J. Cho, Nano Lett. 12 (2012) 4988.
- [20] X. Zhu, Y. Zhu, S. Murali, M.D. Stoller, R.S. Ruoff, ACS Nano 5 (2011) 3333.
- [21] S. Bai, S. Chen, X. Shen, G. Zhu, G. Wang, RSC Adv. 2 (2012) 10977.
- [22] Y. Sun, J. Zhang, T. Huang, Z. Liu, A. Yu, Int. J. Electrochem. Sci. 8 (2013) 2918.
- [23] S.L. Chou, J.Z. Wang, D. Wexler, K. Konstantinov, C. Zhong, H.K. Liu, S.X. Dou, J. Mater. Chem. 20 (2010) 2092.
- [24] D. Maiti, M. Krishnan, S. Velaga, P. Sujitha Devi, Cryst. Growth Des. 13 (2013) 3644.
- [25] L. Machala, J. Tucek, R. Jboril, Chem. Mater. 23 (2011) 3255.
- [26] D. Bersani, P.P. Lottici, A. Montenero, J. Raman Spectrosc. 30 (1999) 355.
- [27] H.C. Choi, Y.M. Jung, S.B. Kim, Vib. Spectrosc. 37 (2005) 33.
- [28] X. Xue, W. Ji, Z. Mao, H. Mao, Y. Wang, X. Wang, W. Ruan, B. Zhao, J.R. Lombardi, J. Phys. Chem. C 116 (2012) 8792.
- [29] D.M. Sherman, T.D. Waite, Am. Mineral. 70 (1985) 1262–1269.
- [30] A.A. Akl, Appl. Surf. Sci. 233 (2004) 307.
- [31] L.A. Marusak, R. Messier, W.B. White, J. Phys. Chem. Solids 41 (1980) 981.
- [32] T. Wang, S. Zhou, C. Zhang, J. Lian, Y. Liang, W. Yuan, New J. Chem. 38 (2014) 46.
- [33] L.B. Wang, L.X. Song, Z. Dang, J. Chen, J. Yang, J. Zeng, Cryst. Eng. Comm. 14 (2012) 3355.
- [34] A. Banerjee, V. Aravindan, S. Bhatnagar, D. Mhamane, S. Madhavi, S. Ogale, Nano Energy 2 (2013) 890.
- [35] J.S. Gnanaraj, E. Zinigrad, L. Asraf, M. Sprecher, H.E. Gottlieb, W. Geissler, M. Schmidt, D. Aurbach, Electrochem. Comm. 5 (2003) 946.
- [36] V. Aravindan, J. Gnanaraj, S. Madhavi, H.-K. Liu, Chem. A Eur. J. 17 (2011) 14326.
- [37] G. Wang, T. Liu, Y. Luo, Y. Zhao, Z. Ren, J. Bai, H. Wang, J. Alloys Compd. 509 (2011) L216.
- [38] H. Xiao, Y. Xia, W.K. Zhang, H. Huang, Y.P. Gan, X.Y. Tao, J. Mater. Chem. A 1 (2013) 2307.
- [39] B. Wang, J.S. Chen, H.B. Wu, Z.Y. Wang, X.W. Lou, J. Am. Chem. Soc. 133 (2011) 17146.
- [40] J.S. Chen, T. Zhu, X.H. Wang, H.G. Yang, X.W. Lou, J. Am. Chem. Soc. 132 (2010) 13162.
- [41] S. Zeng, K. Tang, T. Li, Z. Liang, W. Zhou, J. Phys. Chem. C 111 (2007) 10217.
- [42] X. Li, L. Qiao, D. Li, X. Wang, W. Xie, D. He, J. Mater. Chem. A 1 (2013) 6400.